Available online at www.sciencedirect.com
ScienceDirect
Journal of Solid State Chemistry 180 (2007) 3443–3449
JOURNAL OF SOLID STATE CHEMISTRY
www.elsevier.com/locate/jssc

Synthesis and characterization of nanoparticulate MnS within the pores of mesoporous silica

Louse Barry[a], Mark Copley[a], Justin D. Holmes[a,b], David J. Otway[a], Olga Kazakova[c], Michael A. Morris[a,b,*]

[a]*Department of Chemistry, University College Cork, Cork, Ireland*
[b]*Centre for Research on Adaptive Nanostructures and Nanodevices (CRANN), Trinity College Dublin, Dublin 2, Ireland*
[c]*National Physical Laboratory, Teddington, UK*

Received 24 July 2007; received in revised form 2 October 2007; accepted 3 October 2007
Available online 7 October 2007

Abstract

Mesoporous silica was loaded with nanoparticulate MnS via a simple post-synthesis treatment. The mesoporous material that still contained surfactant was passivated to prevent MnS formation at the surface. The surfactant was extracted and a novel manganese ethylxanthate was used to impregnate the pore network. This precursor thermally decomposes to yield MnS particles that are smaller or equal to the pore size. The particles exhibit all three common polymorphs. The passivation treatment is most effective at lower loadings because at the highest loadings (SiO_2:MnS molar ratio of 6:1) large particles (>50 nm) form at the exterior of the mesoporous particles. The integrity of the mesoporous network is maintained through the preparation and high order is maintained. The MnS particles exhibit unexpected ferromagnetism at low temperatures. Strong luminescence of these samples is observed and this suggests that they may have a range of important application areas.

Keywords: MnS; Mesoporous silica; Nanoparticles; Magnetism

1. Introduction

The constrained growth of metal and semiconductor nanoparticles and nanowires within the nanoscale channels of mesoporous silica materials [1] has been keenly researched. Ordered mesoporous materials are ideal templates because of their uniform pore size, highly periodic structures, dense pore packing as well as high chemical and thermal stability. Thus, these 'nanomolds' confer the ability to control nanoparticulate size, shape and organization. In Cork we have pioneered the use of these materials to form semiconductor and other inorganic nanowires [2–4]. Several studies have explored the preparation of metal sulfides using mesoporous silica powder/film templates including CdS [5], ZnS [6] and PbS [7]. Shi et al. [8] have reviewed a range of methods for the incorporation of sulfide materials into ordered mesoporous materials.

Sulfides are an important class of semiconductors. Manganese sulfide (MnS) has a number of potential applications based on its magnetic properties and wide bandgap energy (3.2 eV) [9]. It may have importance as a dilute magnetic semiconductor [10], in solar cells [11] and various other applications [12]. Importantly, luminescent properties of nanocrystalline MnS in silica xerogels have been demonstrated [13]. In all of these applications, control of particle size, shape and crystallography is of strict importance and, thus, the synthesis of the MnS is critical. Various preparation methodologies have been used including chemical bath deposition [14], solvothermal routes [15] and molecular beam epitaxy (MBE) [16]. In order to produce well-defined MnS materials, we have adapted a mesoporous silica templating route coupled to the use of novel xanthate precursors (as previously developed for

*Corresponding author. Department of Chemistry, University College Cork, Cork, Ireland.
E-mail address: m.morris@ucc.ie (M.A. Morris).

0022-4596/$ - see front matter © 2007 Elsevier Inc. All rights reserved.
doi:10.1016/j.jssc.2007.10.004

ZnS preparation [17]). These single source metal sulfide precursors are attractive as they are air-stable, suitable for the synthesis of a wide range of metal sulfides and should facilitate high yields and stoichiometric control. The results presented here demonstrate the practicality of this synthesis strategy.

2. Experimental

2.1. Sample preparation

All chemicals $MnCl_2 \cdot 4H_2O$, *N*,*N*,*N*′-tetramethylenediamine (TMEDA), potassium *O*-ethylxanthate [K(Xan)], tetraethoxysilane (TEOS), trimethylchlorosilane (TMCS) and solvents were supplied by Aldrich Chemical Co. and used as-received. The Pluronic^{TM} non-ionic polyethylene oxide–polypropylene oxide–polyethylene oxide triblock copolymer ($EO_{20}PO_{69}EO_{20}$) was used as the structural directing agent (SDA) in mesoporous silica formation. Manganese ethylxanthate (Mn[$(S_2COEt)_2$]TMEDA) was synthesized by a method modified from Cusack et al. [18]. TMEDA (0.58 g, 5 mmol, 0.75 ml) was added to an aqueous solution of $MnCl_2 \cdot 4H_2O$ (0.990 g, 5 mmol) while stirring. An aqueous solution of K(Xan) (1.60 g, 10 mmol) was added drop wise to this mixture and stirred for 30 min. The solid was recovered by filtration and washed copiously with water before being dried under vacuum for 12 h. The manganese ethylxanthate product was confirmed by elemental analysis (within 0.1 wt%), infra-red spectroscopy and ^{1}H NMR spectroscopy. Following characterization, the Mn[$(S_2COEt)_2$]TMEDA was dispersed in 30 ml of dry tetrahydrofuran (THF) while stirring under nitrogen.

The synthesis of P123 templated mesoporous silica (meso-SiO_2) was adapted from a previously described method [1]. 4.0 g P123 in 120 ml of 2 M HCl and 30 ml H_2O was stirred for 30 min. The mixture was subsequently placed in a water bath and heated to 40 °C. 11.3 g of TEOS was added. The solution was stirred at this temperature for 24 h; after this period, it was placed in an oven (60 °C) for 5 days. This permits the silica to reproduce the surfactant network. The material was recovered after drying and the P123 SDA was not removed. The as-recovered samples were treated by immersion in TMCS which selectively passivated the external surface (pores are not available because of the presence of surfactant). The surfactant template was then removed by solvent extraction to expose untreated pore wall surface area. The functionalized mesoporous material (0.25 g) was then added to about 100 ml of THF. To this mixture, the Mn[$(S_2COEt)_2$]TMEDA–THF solution was added and heated at the reflux temperature for 24 h. After this time, the product was recovered by filtration and dried under vacuum for 12 h. The composite sample was then heated in a nitrogen atmosphere to 450 °C at a ramp rate of 2 °C min^{-1} for 12 h. The procedure was repeated using various loadings of the ethylxanthate precursor.

2.2. Characterization methods

Microanalyses were recorded on an Exeter Analytical Inc. CE444 CHN elemental analyzer. ^{1}H nuclear magnetic resonance spectroscopy (NMR) data were obtained in $CDCl_3$ solution at ambient temperature using a Bruker-Arance 300 spectrometer with TMS as an internal standard. Diffuse reflection Fourier transform infra-red spectroscopy (DRIFTS) data sets were recorded on a Bio-Rad Digilab FTS-3000 in the region 4000–500 cm^{-1}. High and Low angle XRD measurements were performed with a Philips X'Pert diffractometer using Cu$K\alpha$ radiation with an anode current of 40 mA and an accelerating current of 40 kV N_2 adsorption–desorption experiments were performed using a Micromeritics Gemini 2375 volumetric analyzer. The samples were pretreated at 200 °C for 4 h, and the specific surface area of the samples was determined using the Brunauer–Emmett–Teller (BET) method. The pore volume and pore size distribution were derived from the desorption profiles of the isotherms using the Barrett–Joyner–Halanda (BJH) method. The transmission electron microscopy (TEM) micrographs were collected using a JEOL JEM-200 FX microscope operated at 200 kV. The sample was dispersed in absolute ethanol, sonicated and dropped onto copper grids coated with a holey carbon film. Magnetization measurements were performed using a commercial SQUID (superconductor quantum interference device) magnetometer (MPMS XL, Quantum Design) at temperatures between 1.8 and 370 K and in fields up to 30 kOe. Fluorescence spectra were recorded on a Perkin-Elmer LS 50B spectrophotometer following sonication of the samples in absolute ethanol.

3. Results and discussion

Thermogravimetric analysis shows strong weight loss on heating consistent with the conversion of the manganese ethylxanthate to MnS. Confirmation of this can be seen in DRIFTS spectra shown in Fig. 1. The starting material [Mn$(S_2COEt)_2$TMEDA] shows three strong bands in the region 1190–1035 cm^{-1} which are characteristic of xanthate complexes [18]. More specifically these bands are due to vibrations from ν(C–S), ν(Et–O) and ν(C–O). A band at 2900 cm^{-1} is representative of ν(C–H). The characteristic frequency of ν(C–N) is present at 1460 cm^{-1}. Bands present around 2800–3000 cm^{-1} represent O–H related vibrations from H_2O in the air. Mn presence was confirmed by EDX measurements. Preparation of the MnS-loaded meso-SiO_2 is accompanied by a loss of all the xanthate related features. Broad bands present at ~3000–3500 cm^{-1} and ~1630 cm^{-1} are attributed to the stretching vibration of hydroxyl and water at the silica surface, respectively [19]. A Si–C stretching mode is also seen at 830 cm^{-1} and this can be assigned to the presence of Si–CH_3 groups suggesting that the silylation treatment of the silica surface was effective.

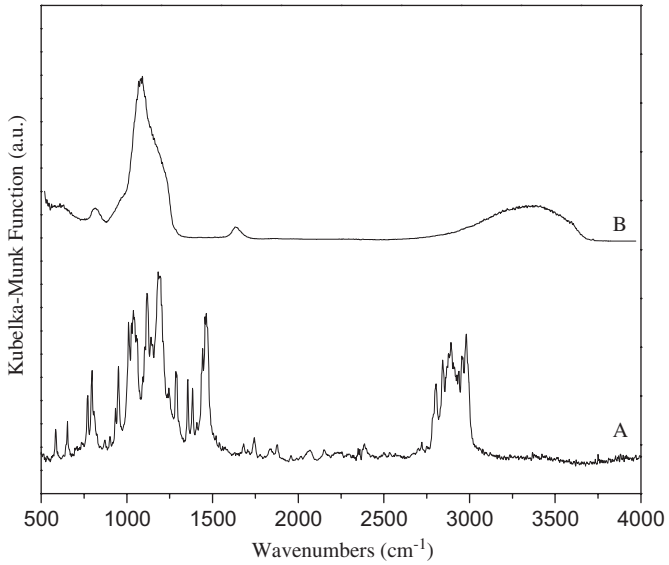

Fig. 1. DRIFTS spectra of (A) MnS xanthate complex as-prepared and (B) the MnS-loaded meso-SiO_2 material after calcinations.

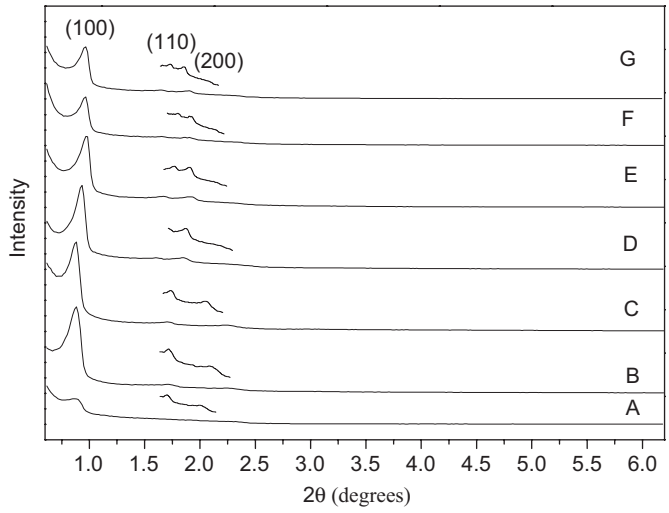

Fig. 2. Low angle XRD patterns of meso-SiO_2 at various preparation stages: (A) as synthesized, (B) TMCS passivated and (C) passivated sample after surfactant extraction. (D)–(G) XRD of calcined MnS–meso-SiO_2 with a SiO_2:MnS precursor molar ratios of (D) 50:1, (E) 25:1, (F) 8:1 and (G) 6:1. Expanded data are shown to reveal the (1 1 0) and (2 0 0) reflections.

Fig. 2 shows the low angle XRD patterns of each preparation stage for functionalized meso-SiO_2, and of the MnS impregnated samples. All samples display three low angle reflections labeled as (1 0 0), (1 1 0) and (2 0 0) and are readily assigned to the P123 hexagonally packed pore arrangements [1]. It is clear from the data that a well-ordered pore arrangement is maintained even at the highest levels of doping used here (molar ratio of SiO_2:MnS of 6:1). Note that an increase in peak intensity is observed and shown explicitly in Fig. 2(A) and (B) due to the partial removal of the surfactant phase in the reflux conditions used. This is due to the increased X-ray scattering contrast between the pores and the walls. Between the data sets (C) and (G) in Fig. 2 there is a progressive decrease in the reflection intensity as the MnS content increases. This is consistent with pore filling because of the reduction in the X-ray scattering contrast between the pores and the walls of the mesoporous material [7]. The important crystal parameters of the calcined materials are detailed in Table 1. It can be seen that inclusion of MnS occurs with a decrease of the unit cell parameter. This is possibly due to the MnS promoting increased silicate condensation during the calcination process.

Fig. 3 shows the nitrogen adsorption–desorption isotherms for the pretreated meso-SiO_2 and the MnS-loaded samples. All the isotherms are of IUPAC type IV and clearly demonstrate the mesoporous nature of the materials. The effect of MnS noted in XRD data can also be seen in the increase in the pore volume and surface area between the unloaded and loaded sample and it is suggested this is due to promotion of the removal of the last traces of surfactant. Thereafter, as the MnS content increases there is a progressive decrease in surface area and pore volume. This is in strong agreement with the assertion that MnS is being formed within the pore network. Note also that the pore diameter does not vary (within experimental error) with Mn content (apart from a small increase between unloaded and loaded materials due to surfactant removal as outlined above).

On close inspection of Fig. 3, it can be seen that the isotherms show shape changes as a function of loading. As the MnS content increases, the isotherm can be seen to be stepped and consists of a combination of two individual adsorption processes. This is indicative of the loading producing two different pore sizes. Similar effects have

Table 1
Physiochemical characteristics of calcined meso-SiO_2 and MnS–meso-SiO_2 materials

Molar ratio SiO_2:MnS	Surface area (cm^3/g)	Pore volume (cm^3/g)	Pore diameter (Å)	*d* spacing (Å)	Unit cell (Å)	Wall thickness (Å)
∞	477	0.62	66.1	99.91	115.36	49.26
50	845	0.83	67.7	94.46	109.07	41.37
25	718	0.69	67.7	90.36	104.33	36.63
8	642	0.65	67.5	91.41	105.56	38.06
6	441	0.45	67.7	91.18	105.28	37.58

Pore diameter derived from adsorption data. Wall thicknesses calculated by: unit cell−pore diameter (unit cell = $2 \times d(10)\sqrt{3}$).

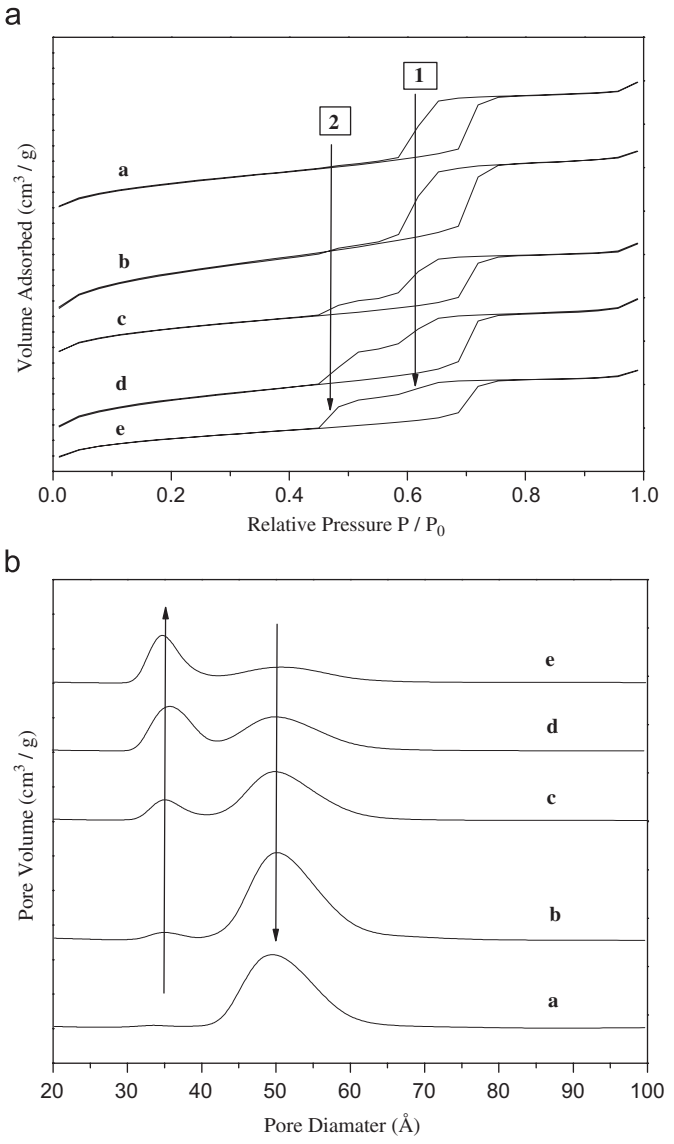

Fig. 3. Top: Nitrogen adsorption–desorption isotherms of (a) unloaded meso-SiO_2 and MnS–meso-SiO_2 samples with a SiO_2:precursor molar ratios of (b) 50, (c) 25, (d) 8 and (e) 6. Figs. 1 and 2 indicate two different adsorption processes that occur for the MnS-loaded samples. Bottom: Isotherm derived pore volume versus pore diameter plots of the same samples.

been seen experimentally for silica blocking of pores [20] and has been studied theoretically [21]. This is shown explicitly in Fig. 3 using BJH data from the desorption data (since this is more sensitive than adsorption data to degree of pore filling). Two distinct pore sizes of 3.5 and 5 nm are explicitly shown; as the MnS content increases, there is a commensurate decrease of the large pore size feature and increase in the small pore size feature. It is concluded that the 5 nm diameters are consistent with open pores with no MnS present while the 3.5 nm pores contain discrete MnS nanoparticles around 1.5 nm in diameter.

The retention of good hexagonal pore ordering of the silica and the presence of MnS particles can be demonstrated using TEM. Typical data are shown in Fig. 4. In Fig. 4A TEM micrographs of the meso-SiO_2 following surfactant extraction show the presence of an extended pore system. The pores are essentially straight and show only faint signs of internal materials which are presumably remaining surfactant. The average pore diameter is measured at about 7 nm, in good agreement with nitrogen adsorption–desorption data. On MnS incorporation (Fig. 4B) the pores become grayer and accumulation of small particles can be seen. At the highest loadings, the internal MnS particles can be seen readily as well as external (to the particle) MnS deposits that appear at these high contents and are much larger (>50 nm) than the internal particles (1–5 nm). In Fig. 4C these large particles are indicated by the arrows and clearly these are formed at the surface of the meso-SiO_2 particles. That these only appear at high loadings suggests that the silylation treatment to preferentially place material inside the pores was successful. EDX confirms the presence of MnS. Cu (support grid), Si and O features can also be seen. Comparison of signal heights to an MnS standard confirms the stoichiometry as Mn:S = 1:1.

As might be imagined for small particles that are limited in size by the pore diameter, XRD data result in diffractograms with broad features and high background. The profile is complex but features (as shown in Fig. 5) can be readily assigned to the rock salt (α-phase, JCPDS card number 72-1534), zinc blende (β-phase, JCPD card number 88-2223) and wurtzite (γ-phase, JCPDS card number 40-1289) polymorphs of the MnS structure. The silica matrix plays a role in determining the phase exhibited as similar treatment of the ethylxanthate produces larger (200 nm particles) of pure zinc blende structure (inset in Fig. 5). This is probably related to the pore structure limiting particulate growth and particle size can determine the relative stability of polymorphic structures [22]. Simple Scherrer analysis is problematical because of the contribution from different polymorphs and experimentally peak widths vary from 1.05° to 1.5° 2θ. The MnS crystallite size is estimated to be between 3.5 and 5.1 nm, i.e. smaller or equal to the pore diameter. These data suggest that the particle size has been limited by the pore diameter.

The MnS-loaded meso-SiO_2 samples show interesting magnetic properties. These properties are briefly described here but detailed analysis is beyond the scope of the present paper. All three polymorphs of MnS are reported as antiferromagnetic with a Nèel temperature in the range 75–150 K [23]. In order to investigate the magnetic properties of these nanodimensioned particles confined within a mesoporous template, measurements were performed using a magnetometer. Fig. 6 shows the zero-field-cooled (ZFC) and field-cooled (FC) magnetization curves in the range of 0–300 K obtained for an MnS–SiO_2 sample with a SiO_2:MnS molar ratio of 6:1. Similar data were recorded at lower loadings but are not shown here for clarity. The ZFC plot displays a clear peak at 42 K due to transition between ferromagnetic and superparamagnetic behavior. The peak occurs at a temperature know as the

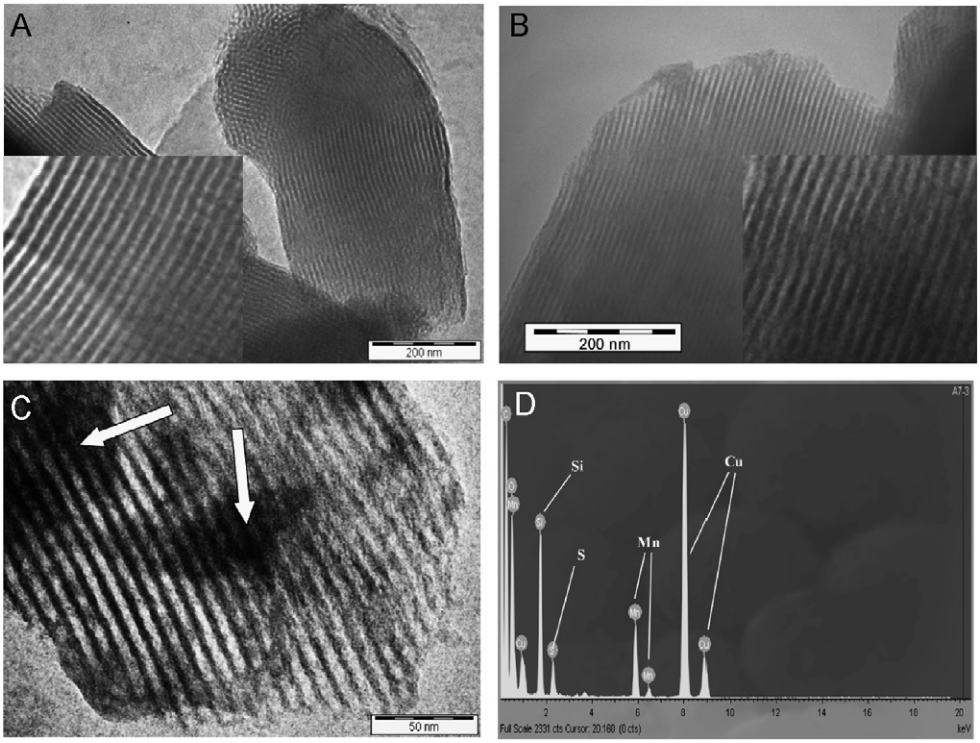

Fig. 4. TEM micrographs of unloaded (A) and MnS-loaded (B and C) mesoporous matrices. The SiO_2:MnS precursor molar ratios of (B) 50:1 and (C) 6:1 are shown. Typical EDX spectrum indicating the presence of MnS is shown in (D). The insets of (A) and (B) are magnifications of the data for illustrative purposes.

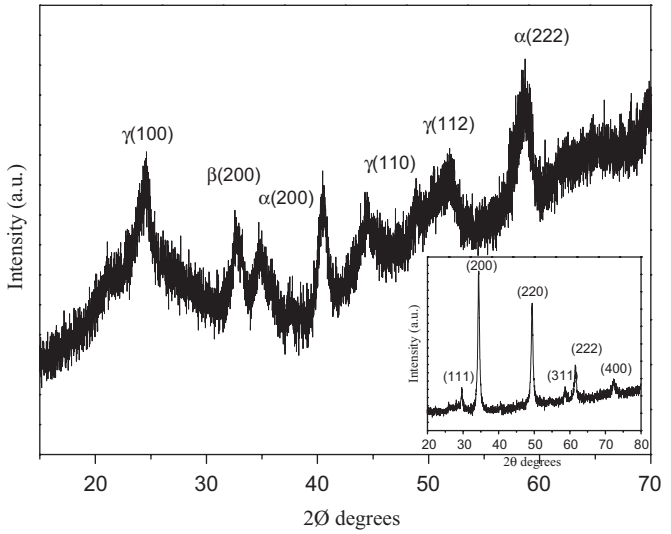

Fig. 5. High angle XRD pattern of MnS (Mn:SiO_2 molar ratio of 8:1) incorporated meso-SiO_2 sample. The inset shows data from manganese ethylxanthate after similar thermal treatment.

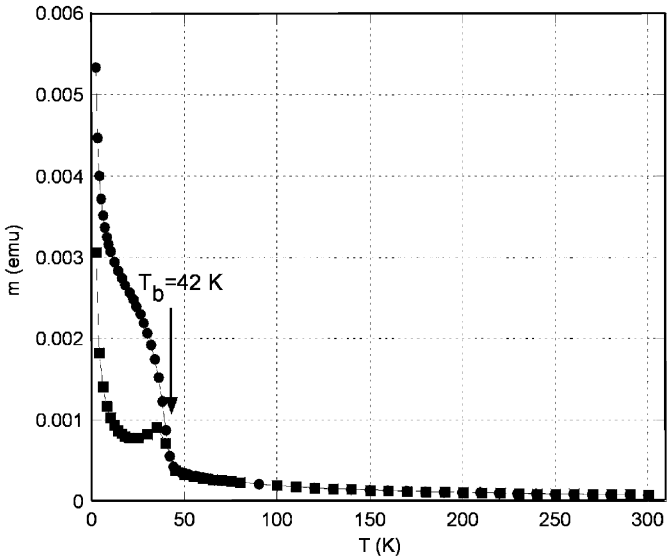

Fig. 6. (■) Zero-field-cooled (ZFC) and (●) field-cooled (FC) magnetization versus temperature plots for an MnS–SiO_2 sample at an external magnetic field of 500 Oe.

blocking temperature, T_b (42 K). This is the first time such behavior has been seen for nanoscale MnS particles. The transition occurs when the thermal energy becomes greater than the barrier height for magnetization reversal and these observations suggest the materials contain a ferromagnetic component. This weak ferromagnetic component is probably due to ferromagnetic ordering of excess surface spins that become more important at the dimensions observed here [24]. As can be seen here the net magnetization increases with decreasing temperature. This is because thermal fluctuations decrease with decreasing temperature and the spins can align with the applied field [25]. If the inter-particulate magnetic coupling was strong the interaction would be such to stabilize the spins in their original

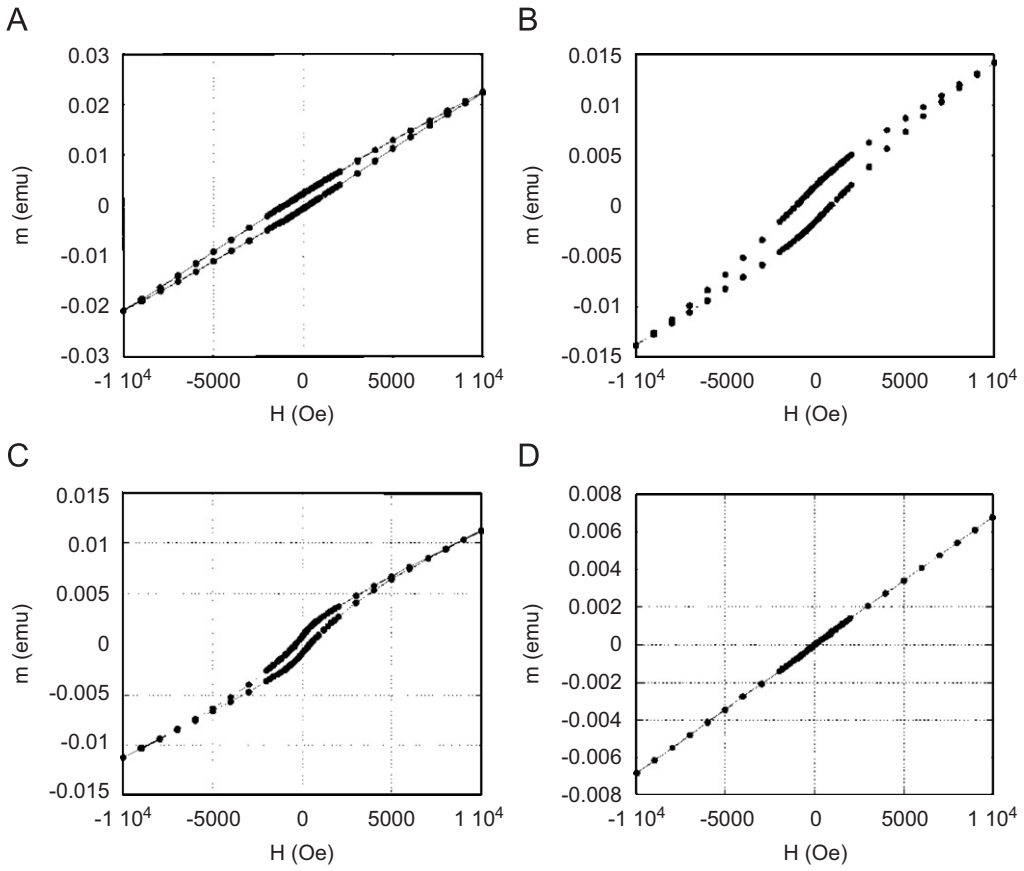

Fig. 7. Magnetic hysteresis loops of MnS-loaded meso-SiO_2 at 10 (A), 25 (B), 35 (C) and 50 (D) K.

conformation thus overcoming low temperature alignment with the magnetic field (although other explanations are possible this seems the most likely to us). Further evidence of the lack of inter-particle coupling is observed by examining the temperature occurrence of the blocking temperature. A low blocking temperature (42 K) suggests a lack of coupling to suppress thermal fluctuations of the magnetic spins. The FC and ZFC curves overlap at high temperatures and begin to separate ~44 K, indicating the blocking temperature of the largest particles. The closeness of the T_b to the temperature where the ZFC and FC curves separate indicates the presence of nanoparticles with a narrow size distribution [26] as is also suggested by the narrow widths of the BJH plots shown in Fig. 3.

The presence of the ferromagnetic phase in these samples is more explicitly shown in the magnetic hysteresis loops shown in Fig. 7. It is clear that data recorded at 25 and 35 K illustrate profiles typical of weak ferromagnetic behavior. Above the blocking temperature, the ferromagnetic component is lost as seen by the hysteresis curves recorded at 50 K and the material displays a paramagnetic behavior. The nature of the dominant paramagnetic behavior at 10 K can also be clearly seen in the data provided.

The MnS-loaded meso-SiO_2 materials show strong photoluminescence. Typical data (sample has a SiO_2:MnS molar ratio of 25:1) is shown in Fig. 8 but all doped materials behave similarly. The feature at 583 nm can be assigned directly to the $^4T_1 \rightarrow {}^6A_1$ transition in Mn^{2+} [13]. Previous authors have shown strong Mn^{2+} luminescence in silica sol–gels co-doped with CaS and MnS but to our knowledge this is the first observation of strong luminescence in singly doped silica systems.

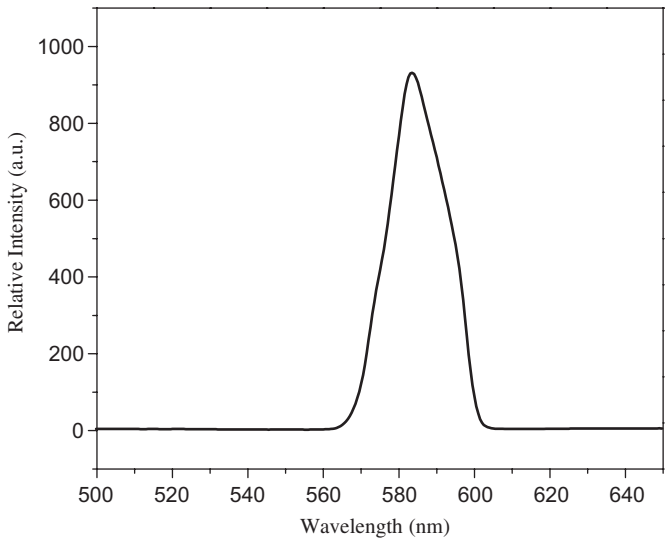

Fig. 8. Photoluminescence spectra of MnS-loaded meso-SiO_2 (SiO_2:MnS molar ratio of 25:1).

4. Conclusions

This paper presents evidence that xanthate-based precursors are useful for the synthesis of sulfides. In this approach, the methods have been extended to the inclusion of sulfides into mesoporous materials. The use of a silylating agent to passivate the exterior surface and thus promote precursor decomposition within the pores was effective at all but the highest loadings. This allows well-dispersed particles to be formed without exterior pore blocking. This passivation method may prove to be a useful method for the synthesis of advanced catalysts. The pores within the mesoporous matrix appear to prevent particle agglomeration enabling a small particle size to be maintained through a 450 °C heating cycle. There is no indication of pore collapse during the loading process or on subsequent calcination. The particles have interesting magnetic properties. MnS particles in the silica matrix show weak ferromagnetic properties around 35 K. This effect is related to small nanoparticulate size. The particles within the pores appear to be only weakly magnetically coupled. It is clear from these studies that the magnetic properties of nanoparticles are difficult to predict and require extensive study.

In contrast to previous authors [13], we report strong emission from these materials and suggest that mesoporous silica is much more effective than simple sol–gel materials in enhancing luminescence. The ease of preparation of these materials and the nature of the luminescence demands that potential applications of these samples should be explored.

Acknowledgments

IRCSET is thanked for student support of Louise Barry. Intel, Ireland is also acknowledged for their financial support. SFI is thanked for assistance in purchasing equipment.

References

[1] D. Zhao, J. Feng, Q. Huo, N. Melosh, G.H. Fredrickson, B.F. Chmelka, G.D. Stucky, Science 279 (1998) 548–552.
[2] T.A. Crowley, K.J. Ziegler, D.M. Lyons, D. Erts, H. Olin, M.A. Morris, J.D. Holmes, Chem. Mater. 15 (2003) 3518–3522.
[3] N. Petkov, B. Platschek, M.A. Morris, J.D. Holmes, T. Bein, Chem. Mater. 19 (2007) 1376–1381.
[4] G. Audoit, J.S. Kulkarni, M.A. Morris, J.D. Holmes, J. Mater. Chem. 17 (2007) 1608–1613.
[5] Y. Shan, L. Gao, Mater. Chem. Phys. 89 (2005) 412–416.
[6] W.H. Zhang, J.L. Shi, H.R. Chen, Z.L. Hua, D.S. Yan, Chem. Mater. 12 (2001) 648–654.
[7] F. Gao, Q. Lu, X. Liu, Y. Yan, D. Zhao, Nano Lett. 1 (2001) 743–748.
[8] J.L. Shi, Z.L. Hua, L.X. Zhang, J. Mater. Chem. 14 (2004) 795–806.
[9] S.H. Kan, I. Felner, U. Banin, Isr. J. Chem. 41 (2001) 55–62.
[10] C. Gümüş, C. Ulutuş, Y. Ufuktepe, Opt. Mater. 29 (2007) 1183–1187.
[11] Y. Cheng, Y. Wang, C. Jia, F. Bao, J. Phys. Chem. B 110 (2006) 24399–24402.
[12] A.P. Allivisatos, Science 271 (1996) 933–937.
[13] P. Yang, M. Lu, C. Song, F. Gu, S. Liu, D. Xu, D. Yuan, X. Cheng, J. Non-Cryst. Solids 311 (2002) 99–103.
[14] C.D. Lokhande, A. Ennaoui, P.S. Patil, M. Giersig, M. Muller, K. Diesner, H. Tributsch, Thin Solid Films 330 (1998) 70–75.
[15] S. Lei, K. Tang, Q. Yang, H. Zheng, Eur. J. Inorg. Chem. 20 (2005) 4124–4128.
[16] M. Okajima, J. Tohda, J. Crystal Growth 117 (1992) 810–815.
[17] D. Barreca, E. Tondello, D. Lydon, T.R. Spalding, M. Fabrizio, Chem. Vap. Depos. 9 (2003) 93–98.
[18] J. Cusack, M.G.B. Drew, T.R. Spalding, Polyhedron 23 (2004) 2315–2321.
[19] J. Yang, J. Zhang, L. Zhu, S. Chen, Y. Zhang, Y. Tang, Y. Zhu, Y. Li, J. Hazard. Mater. B 137 (2006) 955–958.
[20] P.V.D. Voort, P.I. Ravikovitch, K.P. Jong, A.V. Neimark, A.H. Janssen, M. Benjelloun, E.V. Bavel, Chem. Commun. 9 (2002) 1010–1011.
[21] P.I. Ravikovitch, A.V. Neimark, Langmuir 18 (2002) 9830–9837.
[22] D.J. Reidy, J.D. Holmes, M.A. Morris, J. Eur. Ceram. Soc. 26 (2006) 1434–1527.
[23] R.I. Hinesy, N.L. Allany, G.S. Bellz, W.C. Mackrodt, J. Phys.: Condens. Matter 9 (1997) 7105–7118.
[24] Y. Wang, C.M. Yang, W. Schmidt, B. Spliethoff, E. Bill, F. Schuth, Adv. Mater. 17 (2005) 53–56.
[25] A.F. Gross, M.R. Diehl, K.C. Beverly, E.K. Richman, S.H. Tolbert, J. Phys. Chem. B 107 (2003) 5475–5482.
[26] G. Clavel, Y. Guari, J. Larionova, C. Guérin, New J. Chem. 29 (2005) 275–279.